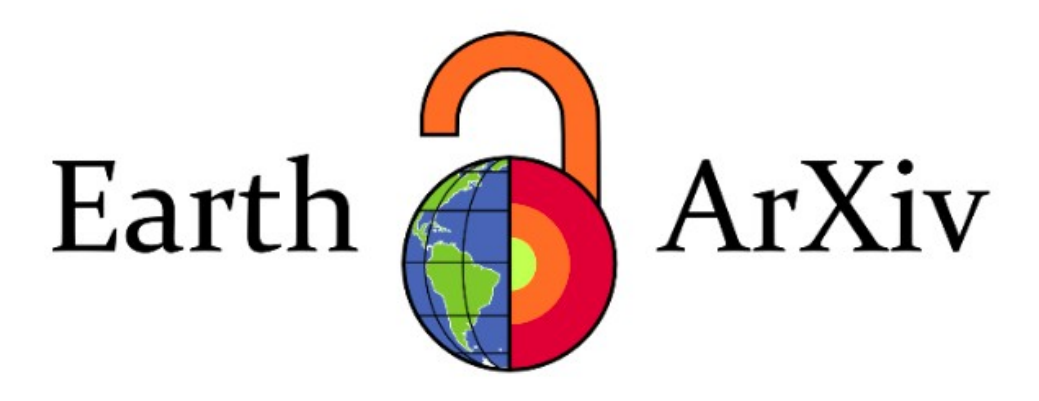
This is a non-peer reviewed preprint submitted to EarthArXiv



Subsequent peer-reviewed versions of this manuscript may have slightly different content. The authors welcome feedback.

Statistical Characterization of LGM and Late Holocene Oceanography in the Indonesian Maritime Continent

- Daffa Z. Mazdhania^{1,2}, Sandy H. S. Herho^{2,3,*}, Iwan P. Anwar^{1,2}, Marfasran
- ⁵ Hendrizan⁴, Siti N. Kaban⁵, Faruq Khadami¹, Rima Rachmayani¹, and Sri Y.
- **6 Cahyarini**⁴
- ⁷ Applied and Environmental Oceanography Research Group, Bandung Institute of
- Technology (ITB), Bandung, West Java, Indonesia 40132
- ⁹ Samudera Sains Teknologi (SST) Ltd., Bandung, West Java, Indonesia 40151
- ³Department of Earth and Planetary Sciences, University of California, Riverside, CA,
- 11 USA 92521
- ⁴Paleoclimate and Paleoenvironment Research Group, Research Center of Climate and
- 13 Atmosphere, National Research and Innovation Agency (BRIN), Bandung, West Java,
- 14 Indonesia 40135
- ¹⁵ Financial Engineering Program, WorldQuant University, Washington, D.C., USA 20002
- ¹⁶ Corresponding author:
- ¹⁷ Sandy H. S. Herho*
- 18 Email address: sandy.herho@email.ucr.edu

ABSTRACT

This study provides a statistical characterization of surface oceanography in the Indonesian Maritime Continent (IMC) during the Last Glacial Maximum (LGM; 23–19 ka) and Late Holocene (LH; 4–0 ka). Using the IgmDA v2.1 paleoclimate data assimilation product, we analyze sea surface temperature (SST), sea surface salinity (SSS), and seawater δ^{18} O. Results indicate the LGM was significantly cooler, saltier, and isotopically enriched, with reduced spatial heterogeneity compared to the LH. Comprehensive nonparametric testing confirms these differences reflect fundamental changes in distributional properties, not merely mean-state shifts. The findings suggest a major oceanographic regime shift, likely driven by lower sea levels, a weakened ITF, enhanced stratification, and a drier regional climate during the LGM. This work offers a statistical framework for understanding IMC sensitivity to glacial-interglacial forcing.

Indonesian Maritime Continent, Last Glacial Maximum, Nonparametric hypothesis testing, Paleoceanography, Probability density estimation

1 INTRODUCTION

The Indonesian Maritime Continent (IMC) represents one of the most critical choke points in the global ocean circulation system. Situated at the heart of the tropical warm pool, the IMC serves as the primary conduit for heat and freshwater exchange between the Pacific and Indian Oceans through the Indonesian Throughflow (ITF) (Gordon, 2005). This interbasin transfer not only influences regional climate patterns but also modulates global thermohaline circulation, making the IMC a pivotal component of Earth's climate machinery.

The complex archipelagic geometry of the modern IMC, however, represents a geologically transient state. During the Last Glacial Maximum (LGM) approximately 23,000 to 19,000 years ago, global sea level stood approximately 120 meters lower than present due to the expansion of continental ice sheets (Clark et al., 2009). This eustatic lowstand exposed the vast continental platform of the Sunda Shelf, creating an extensive landmass known as Sundaland that connected Sumatra, Java, and Borneo to mainland Asia (Voris, 2000; Solihuddin, 2014). The paleogeographic reconstruction by Voris (2000)

demonstrates how this emergence radically altered coastline configuration and drainage patterns across the region.

The progressive flooding of Sundaland during the deglacial period represented a fundamental reorganization of the region's physical geography. Hanebuth et al. (2000) documented the rapid inundation of the Sunda Shelf, identifying meltwater pulse 1A at approximately 14,000 years BP as a particularly rapid phase of transgression. This drowning process continued through the Holocene, with Solihuddin (2014) proposing a five-stage model that culminated in a mid-Holocene highstand approximately 4,000 years ago. The restoration of maritime connections between ocean basins during this transgression necessarily reconfigured surface oceanographic pathways and processes.

While Indonesia's tectonic framework is characterized by active margins and complex plate boundaries [Hall] [2009], the core of the Sunda Shelf has remained relatively stable over the Quaternary period [Tjia] and Liew. [1996]). This tectonic stability makes the region an ideal natural laboratory for isolating the oceanographic signatures of eustatic sea-level change from tectonic influences. The region's classification as a "far-field" location relative to former ice sheets further minimizes complications from glacio-isostatic adjustments (Lambeck et al., [2002]), allowing for clearer interpretation of sea-level proxies.

Existing proxy-based studies provide valuable insights into LGM conditions in the IMC. DiNezio et al. (2018) used climate model simulations to suggest enhanced zonal SST gradients and strengthened trade winds during the LGM, while Larasati et al. (2024) documented cooler temperatures and higher salinities in the Makassar Strait based on marine sediment cores. However, these discrete proxy records, while invaluable, cannot fully characterize the region-wide statistical structure of oceanographic fields or quantitatively describe the nature of distributional changes between climatic states.

The emergence of paleoclimate data assimilation products represents a significant advancement in paleoceanographic reconstruction. By synthesizing spatially heterogeneous proxy networks with the dynamical constraints of general circulation models, these products generate physically consistent, spatially complete reconstructions of past climate states (Tierney et al., 2020). The LGM Data Assimilation product (lgmDA v2.1; (Tierney and Osman, 2022)) provides an especially powerful tool for investigating the IMC's glacial-interglacial oceanographic evolution.

This study leverages the lgmDA v2.1 product to conduct a comprehensive statistical characterization of IMC surface oceanography during the LGM (23-19 ka) and Late Holocene (LH; 4-0 ka). We move beyond conventional mean-state comparisons to analyze the complete probability distributions of sea surface temperature (SST), sea surface salinity (SSS), and seawater δ^{18} O. Through the application of nonparametric hypothesis testing, effect size quantification, and information-theoretic metrics, we test for a fundamental regime shift in the IMC's oceanographic character between glacial and interglacial states, linking statistical evidence to the interplay of ice-volume forcing, paleogeographic change, and throughflow reorganization.

2 DATA AND METHODS

2.1 Paleoclimate Data Assimilation Product

We utilized annual mean of SST, SSS, and seawater oxygen isotope composition ($\delta^{18}O_{sw}$) fields from the lgmDA v2.1 (Tierney and Osman) [2022]; [Tierney et al.], [2020]). We extracted two temporal slices—the LGM and LH—over the IMC region ($15^{\circ}S-10^{\circ}N$, $91^{\circ}E-150^{\circ}E$) to characterize regional oceanic conditions across the last deglaciation.

The lgmDA product synthesizes marine geochemical proxy data with isotope-enabled climate model simulations through offline ensemble data assimilation (Tierney et al., 2020). The methodology implements an ensemble square-root Kalman filter (Whitaker and Hamill), 2002) to merge N=956 (LGM) and N=879 (LH) globally distributed marine proxy records—alkenone unsaturation index ($U_{37}^{K'}$), TEX₈₆, planktic foraminiferal Mg/Ca, and $\delta^{18}O_c$ —with spatially complete fields from the isotope-enabled Community Earth System Model version 1.2 (iCESM1.2; Brady et al., 2019). This offline approach yields dynamically consistent, full-field climate estimates under observational constraints while mitigating spatial sampling biases inherent to heterogeneously distributed proxy networks (Hakim et al., 2016; Tardif et al., 2019). Bayesian proxy-system models (Tierney and Tingley, 2018, 2014; Tierney et al., 2019; Malevich et al., 2019) account for seasonal biases and non-climatic influences in proxy formation through explicit forward modeling.

The model prior ensemble consisted of 50-year climatological means from iCESM1.2 time-slice experiments (preindustrial, 3 ka, 18 ka, 21 ka) configured with PMIP4 boundary conditions (Kageyama

et al., 2017). iCESM1.2 explicitly simulates stable water isotope tracers (H₂¹⁸O, HDO) throughout the hydrological cycle (Brady et al., 2019), enabling direct assimilation of $\delta^{18}O_c$ proxies without empirical $\delta^{18}O_{sw}$ -salinity relationships. Version 2.1 reverted to preindustrial boundary conditions without prognostic 100 phenology for the LH slice after v2.0 generated unrealistic Southern Ocean sea ice distributions (Tierney 101 and Osman, 2022). The assimilation applied covariance localization with 12,000 km cutoff radius (Gaspari 102 and Cohn, 1999) to eliminate spurious long-range correlations, and set proxy observation uncertainties 103 to one-fifth of global proxy-system model residual variance based on systematic validation (Tierney 104 et al., [2020]). The posterior ensemble (N=1,000 realizations) demonstrated substantial skill against independent ice core and speleothem $\delta^{18}O_p$ records ($R^2 = 0.64$), validating the assimilated climate 106 state. We analyzed ensemble-mean annual SST, SSS, and $\delta^{18}O_{sw}$ fields on the native iCESM ocean grid 107 representing time-mean LGM (23–19 ka) and LH (4–0 ka) conditions. 108

2.2 Probability Density Estimation

110

111

113

115

116 117

119

120

121

122

123

124

125

126

129 130

131

132

135

137

We employed nonparametric kernel density estimation (KDE) to characterize the probability density functions of SST, SSS, and seawater $\delta^{18}O_{sw}$ for both paleoclimate epochs (Silverman, 1998; Scott, 2015). KDE provides a smooth, continuous estimate of the underlying probability density function without imposing parametric assumptions about the distributional form. This approach is particularly well-suited for exploring the structure of paleoclimate data, which may exhibit multi-modality, skewness, or other departures from standard parametric families.

For a sample $\{x_i\}_{i=1}^n$ of n observations drawn from an unknown probability density f(x), where $x \in \mathbb{R}$ represents the variable of interest (SST, SSS, or $\delta^{18}O_{sw}$), the kernel density estimator is defined as:

$$\hat{f}_h(x) = \frac{1}{nh} \sum_{i=1}^n K\left(\frac{x - x_i}{h}\right),\tag{1}$$

where $K: \mathbb{R} \to \mathbb{R}_+$ denotes the kernel function, a symmetric probability density function satisfying the normalization condition $\int_{-\infty}^{\infty} K(u) du = 1$, and h > 0 represents the bandwidth parameter, which controls the degree of smoothing applied to the density estimate. The bandwidth h plays a critical role in determining the bias-variance tradeoff: smaller values produce undersmoothed estimates with high variance and low bias, while larger values yield oversmoothed estimates with low variance but high bias. The quantity x_i denotes the i-th observation in the sample, and x represents the evaluation point at which the density is estimated.

We utilized the Gaussian (normal) kernel, which is the most commonly employed kernel function due to its mathematical tractability and optimal efficiency properties:

$$K(u) = \frac{1}{\sqrt{2\pi}} \exp\left(-\frac{u^2}{2}\right),\tag{2}$$

where $u = (x - x_i)/h$ represents the standardized distance between the evaluation point x and the data point x_i , scaled by the bandwidth h. The exponential decay ensures that observations closer to the evaluation point receive greater weight in the density estimate, with the influence of distant observations diminishing rapidly.

The bandwidth was optimally selected via Scott's rule (Scott, 2015), a widely-used automatic bandwidth selection method that balances bias and variance under the assumption of approximate normality:

$$h_{\text{Scott}} = n^{-1/(d+4)} \hat{\sigma},\tag{3}$$

where d=1 represents the dimensionality of the data (univariate case for each variable analyzed separately), n is the sample size, and $\hat{\sigma} = \sqrt{n^{-1}\sum_{i=1}^{n}(x_i-\bar{x})^2}$ denotes the sample standard deviation, with $\bar{x} = n^{-1}\sum_{i=1}^{n}x_i$ representing the sample mean. The exponent -1/(d+4) reflects the optimal rate of bandwidth decay as sample size increases, ensuring consistency of the density estimator. While Scott's rule assumes approximate normality, it provides robust performance even for moderately non-normal distributions and serves as a sensible default choice for exploratory density estimation.

To facilitate direct visual comparison of density shapes across the two paleoclimate epochs (LGM and LH) despite potential differences in peak heights, each density estimate was normalized to unity maximum:

$$\tilde{f}(x) = \frac{\hat{f}_h(x)}{\sup_{x \in \mathbb{R}} \hat{f}_h(x)},\tag{4}$$

where $\tilde{f}(x) \in [0,1]$ represents the normalized density, $\hat{f}_h(x)$ is the original kernel density estimate from Equation 1 and $\sup_{x \in \mathbb{R}} \hat{f}_h(x)$ denotes the supremum (maximum value) of the density estimate over the real line, which for the Gaussian kernel occurs at one of the data points or in regions of high data concentration. This normalization ensures that the maximum density value equals unity for all distributions, enabling direct comparison of distributional shapes, modes, and spread without confounding effects from differences in absolute density scales.

All KDE computations were implemented using the scipy.stats.gaussian_kde function from the SciPy library (Virtanen et al.) [2020), which provides an efficient and numerically stable implementation of Gaussian KDE with automatic bandwidth selection. Density evaluations were performed on uniform grids spanning the data range $[\min\{x_i\}, \max\{x_i\}]$ with 200 equally-spaced evaluation points, where $\min\{x_i\}$ and $\max\{x_i\}$ denote the minimum and maximum values in the sample, respectively. This grid resolution was chosen to provide smooth density curves while maintaining computational efficiency.

2.3 Distributional Normality Assessment

Prior to conducting parametric hypothesis tests or making distributional assumptions, we rigorously assessed the normality of our paleoclimate data distributions using a comprehensive battery of five complementary statistical tests. The assessment of normality is critical for determining the appropriateness of parametric versus nonparametric statistical methods, as many classical tests assume normally distributed data. By employing multiple tests with different sensitivities to various types of departures from normality (e.g., skewness, kurtosis, tail behavior), we ensured a robust and comprehensive evaluation.

Let $\{x_i\}_{i=1}^n$ denote a random sample of n observations with hypothesized distribution $F_0 \sim \mathcal{N}(\mu, \sigma^2)$, where $\mathcal{N}(\mu, \sigma^2)$ represents a normal (Gaussian) distribution with mean $\mu \in \mathbb{R}$ and variance $\sigma^2 > 0$. The null hypothesis for all normality tests is $H_0: F = F_0$, stating that the true underlying distribution F of the data is normal, against the alternative hypothesis $H_1: F \neq F_0$, indicating departure from normality.

2.3.1 Shapiro-Wilk Test

The Shapiro-Wilk test (Shapiro and Wilk, 1965) is widely regarded as one of the most powerful omnibus tests for detecting departures from normality, particularly in small to moderate samples ($n \le 5000$). The test evaluates the correlation between the ordered sample values and the expected values of order statistics from a standard normal distribution. The test statistic is constructed as:

$$W = \frac{\left(\sum_{i=1}^{n} a_i x_{(i)}\right)^2}{\sum_{i=1}^{n} (x_i - \bar{x})^2},\tag{5}$$

where $x_{(i)}$ denotes the *i*-th order statistic (the *i*-th smallest value when the sample is arranged in ascending order, such that $x_{(1)} \le x_{(2)} \le \cdots \le x_{(n)}$), $\bar{x} = n^{-1} \sum_{i=1}^{n} x_i$ is the sample mean, and the coefficients a_i for $i = 1, \ldots, n$ are weights derived from the expected values, variances, and covariances of order statistics from a standard normal distribution. These weights are computed through a complex algorithm involving the inverse of the covariance matrix of normal order statistics. The numerator of W represents the squared correlation between the ordered data and expected normal order statistics, while the denominator represents the total sample variance.

Under the null hypothesis $H_0: F = F_0$, the test statistic satisfies $W \in (0,1]$, with values close to unity $(W \approx 1)$ indicating strong agreement with normality. Departures from normality in either tail behavior, skewness, or kurtosis cause W to decrease. The null hypothesis of normality is rejected when $W < W_{\alpha}$, where W_{α} represents the critical value corresponding to the chosen significance level α (typically $\alpha = 0.05$). Critical values are determined from the empirical sampling distribution of W under normality, which depends on the sample size n.

2.3.2 Anderson-Darling Test

183

185

186 187

190

191

193

194

195

206

207

210

211

212

217

219

The Anderson-Darling test (Anderson and Darling, 1952) provides a weighted modification of the Kolmogorov-Smirnov test that places greater emphasis on discrepancies in the distribution tails, making it particularly sensitive to departures from normality in the extremes of the distribution. This characteristic is valuable for paleoclimate data where tail behavior often carries important scientific meaning. The test employs a weighted empirical distribution function (EDF) statistic defined through the integral form:

$$A^{2} = n \int_{-\infty}^{\infty} \frac{[F_{n}(x) - F_{0}(x)]^{2}}{F_{0}(x)[1 - F_{0}(x)]} dF_{0}(x), \tag{6}$$

where n is the sample size, $F_n(x) = n^{-1} \sum_{i=1}^n \mathbb{I}(x_i \le x)$ is the empirical cumulative distribution function (CDF), with $\mathbb{I}(\cdot)$ denoting the indicator function (equal to 1 when the condition is true and 0 otherwise), $F_0(x)$ represents the hypothesized normal CDF, and the weighting function $[F_0(x)[1-F_0(x)]]^{-1}$ in the denominator amplifies deviations in the tails where $F_0(x)$ approaches 0 or 1. The integration with respect to $dF_0(x)$ ensures that the test gives appropriate weight across the entire support of the distribution.

For the case of complete specification with estimated parameters, where $F_0(x) = \Phi\left(\frac{x-\bar{x}}{\hat{\sigma}}\right)$ is the CDF of a normal distribution standardized using the sample mean \bar{x} and sample standard deviation $\hat{\sigma}$, and $\Phi(\cdot)$ denotes the standard normal CDF, the computational form becomes:

$$A^{2} = -n - \frac{1}{n} \sum_{i=1}^{n} (2i - 1) \left[\ln \Phi(z_{(i)}) + \ln(1 - \Phi(z_{(n+1-i)})) \right], \tag{7}$$

where $z_{(i)} = (x_{(i)} - \bar{x})/\hat{\sigma}$ are the standardized order statistics (the ordered sample values transformed to have mean zero and unit variance), i indexes the position in the ordered sample, $\ln(\cdot)$ denotes the natural logarithm, and the term (n+1-i) creates a symmetric pairing that efficiently captures both tail behaviors. The factor (2i-1) weights observations according to their position in the ordered sample. When population parameters are estimated from the data rather than specified a priori, modified critical values must be employed to account for the additional uncertainty introduced by parameter estimation (Stephens, 1974), as standard critical values would lead to conservative tests with reduced power.

2.3.3 Kolmogorov-Smirnov Test

The one-sample Kolmogorov-Smirnov test (Kolmogorov) [1933] Smirnov [1948] provides a nonparametric goodness-of-fit test based on the maximum absolute vertical distance between the empirical and hypothesized cumulative distribution functions. Unlike the Anderson-Darling test, the KS test weights all regions of the distribution equally. The test statistic quantifies the supremum (maximum) deviation:

$$D_n = \sup_{x \in \mathbb{R}} |F_n(x) - F_0(x)|, \tag{8}$$

where $D_n \in [0, 1]$ represents the maximum absolute difference between the empirical CDF $F_n(x)$ and the hypothesized CDF $F_0(x)$, with the supremum taken over all possible values x in the real line \mathbb{R} . Larger values of D_n indicate greater discrepancy between the observed and hypothesized distributions.

For composite hypotheses where the parameters μ and σ of the normal distribution are not specified a priori but rather estimated from the data using the sample mean $\hat{\mu} = \bar{x}$ and sample standard deviation $\hat{\sigma}$, we employ the modified statistic:

$$D_n^* = \sup_{x \in \mathbb{R}} \left| F_n(x) - \Phi\left(\frac{x - \hat{\mu}}{\hat{\sigma}}\right) \right|,\tag{9}$$

where $\Phi(\cdot)$ is the standard normal CDF as defined previously, and the parameters $\hat{\mu}$ and $\hat{\sigma}$ are estimated from the sample data. When testing composite hypotheses with estimated parameters, the standard Kolmogorov-Smirnov critical values are no longer appropriate because parameter estimation from the data makes the empirical CDF artificially closer to the fitted distribution. Therefore, adjusted critical values or *p*-values must be obtained via the Lilliefors correction (Lilliefors) [1967), which accounts for the increased uncertainty and provides appropriate significance levels for the test with estimated parameters.

2.3.4 D'Agostino-Pearson Omnibus Test

The D'Agostino-Pearson test (D'Agostino, 1971) D'Agostino and Pearson, 1973) provides an omnibus test for normality by combining separate tests for skewness (asymmetry) and kurtosis (tail heaviness) into a single test statistic. This approach recognizes that departures from normality can manifest through either asymmetry in the distribution shape or through heavier or lighter tails than expected under normality. The omnibus test statistic combines these two aspects:

$$K^2 = Z_{\sqrt{b_1}}^2 + Z_{b_2}^2,\tag{10}$$

where $Z_{\sqrt{b_1}}$ and Z_{b_2} are transformed versions of the sample skewness and sample kurtosis, respectively, that have been specifically designed through normalizing transformations to follow approximately standard normal distributions $\mathcal{N}(0,1)$ under the null hypothesis of normality. By squaring these standardized statistics and summing them, we obtain a chi-squared distributed test statistic. The sample skewness $\sqrt{b_1}$ and sample kurtosis b_2 are defined as:

$$\sqrt{b_1} = \frac{m_3}{m_2^{3/2}}, \quad b_2 = \frac{m_4}{m_2^2},\tag{11}$$

$$m_k = \frac{1}{n} \sum_{i=1}^{n} (x_i - \bar{x})^k, \tag{12}$$

for k = 2, 3, 4, where m_k denotes the k-th central moment (the k-th moment about the mean), $m_2 = \hat{\sigma}^2$ is the sample variance, m_3 measures asymmetry, and m_4 measures tail weight. The skewness $\sqrt{b_1}$ equals zero for symmetric distributions and takes positive or negative values for right-skewed or left-skewed distributions, respectively. The kurtosis b_2 equals 3 for normal distributions, with $b_2 > 3$ indicating heavier tails (leptokurtic) and $b_2 < 3$ indicating lighter tails (platykurtic) than the normal distribution.

Under the null hypothesis of normality H_0 , the combined statistic follows a chi-squared distribution with two degrees of freedom asymptotically: $K^2 \sim \chi_2^2$ as $n \to \infty$. The two degrees of freedom correspond to the two independent components being tested (skewness and kurtosis). This test requires a minimum sample size of $n \ge 8$ observations to ensure that the moment estimates are sufficiently stable for reliable inference.

2.3.5 Jarque-Bera Test

The Jarque-Bera test (Jarque and Bera, 1980, 1987) provides an alternative omnibus approach to testing normality by combining skewness and kurtosis into a single test statistic. While conceptually similar to the D'Agostino-Pearson test, it employs a simpler functional form that does not require the complex normalizing transformations. The test statistic is:

$$JB = \frac{n}{6} \left(S^2 + \frac{(K-3)^2}{4} \right),\tag{13}$$

where n is the sample size, $S = \sqrt{b_1}$ is the sample skewness as defined in Equation $\boxed{11}$ and $K = b_2$ is the sample kurtosis. The term (K-3) represents the excess kurtosis, which measures the deviation from the normal distribution's kurtosis of 3. The coefficients 6 and 4 in the denominator are chosen such that under the null hypothesis of normality, JB follows asymptotically a chi-squared distribution with two degrees of freedom: $JB \sim \chi_2^2$ as $n \to \infty$. Large values of JB indicate significant departures from normality in either skewness, kurtosis, or both. The test is particularly useful for large samples where the asymptotic distribution provides good approximation to the finite-sample distribution.

All normality tests were implemented via built-in SciPy functions (Virtanen et al.) [2020): shapiro for the Shapiro-Wilk test, anderson for the Anderson-Darling test, kstest for the Kolmogorov-Smirnov test with Lilliefors correction, normaltest for the D'Agostino-Pearson test, and jarque_bera for the Jarque-Bera test. For each variable and epoch combination, we evaluated normality at the conventional significance level $\alpha=0.05$ and considered the data to exhibit non-normal characteristics if the majority (> 50%, i.e., at least three out of five) of the tests indicated statistically significant departure from normality (i.e., p < 0.05). This conservative criterion based on test concordance reduces the likelihood of falsely rejecting normality due to Type I errors from individual tests while ensuring robust detection of genuine non-normality.

2.4 Nonparametric Hypothesis Testing

Given the potential for non-normal distributions in paleoclimate proxy data, we assessed differences between LGM and LH distributions using a comprehensive suite of seven nonparametric hypothesis tests. Nonparametric tests make minimal assumptions about the underlying probability distributions and are robust to outliers, skewness, and heavy tails, making them well-suited for paleoclimate reconstructions where distributional assumptions may be violated. The use of multiple complementary tests with different sensitivities to location, scale, and shape differences ensures comprehensive detection of distributional changes between epochs.

Let $\mathbf{X} = \{X_i\}_{i=1}^{n_1} \overset{\text{i.i.d.}}{\sim} F$ and $\mathbf{Y} = \{Y_j\}_{j=1}^{n_2} \overset{\text{i.i.d.}}{\sim} G$ denote two independent samples of sizes n_1 and n_2 , respectively, drawn from the LGM and LH epochs, where the notation $\overset{\text{i.i.d.}}{\sim}$ indicates that observations are independent and identically distributed according to their respective (unknown) cumulative distribution functions F and G. The subscript i indexes observations from the LGM sample ($i=1,\ldots,n_1$) and j indexes observations from the LH sample ($j=1,\ldots,n_2$). The fundamental null hypothesis for all two-sample tests is $H_0: F=G$, stating that the two distributions are identical, against various alternative hypotheses depending on the specific test.

2.4.1 Mann-Whitney U Test

266

269

270

271

274

275

277

279

280

281

289

290

291

293

296

298

The Mann-Whitney U test (Mann and Whitney) [1947), also known as the Wilcoxon rank-sum test in some contexts, is one of the most widely used nonparametric tests for comparing two independent samples. It tests the null hypothesis $H_0: F = G$ against the one-sided or two-sided alternative that one distribution is stochastically larger than the other, meaning that a randomly selected observation from one population tends to be larger than a randomly selected observation from the other population. The test statistic counts the number of times observations from one sample exceed observations from the other sample:

$$U = \sum_{i=1}^{n_1} \sum_{j=1}^{n_2} \mathbb{I}(X_i > Y_j) = n_1 n_2 + \frac{n_1(n_1 + 1)}{2} - R_1, \tag{14}$$

where $\mathbb{I}(\cdot)$ is the indicator function that equals 1 when the condition $X_i > Y_j$ is true and 0 otherwise, n_1 and n_2 are the sample sizes for the LGM and LH samples respectively, and $R_1 = \sum_{i=1}^{n_1} r_i$ represents the sum of ranks assigned to all observations in sample **X** when both samples are pooled and ranked together from smallest to largest. The rank r_i denotes the position of observation X_i in the combined ordered sample of size $n_1 + n_2$. The alternative computational formula relates U to the rank sum, providing numerical stability and computational efficiency.

Under the null hypothesis $H_0: F = G$, the test statistic U has a known discrete distribution that can be approximated by a continuous normal distribution for sufficiently large samples. The standardized test statistic is:

$$Z = \frac{U - \mu_U}{\sigma_U}, \quad \mu_U = \frac{n_1 n_2}{2}, \quad \sigma_U^2 = \frac{n_1 n_2 (n_1 + n_2 + 1)}{12}, \tag{15}$$

where μ_U represents the expected value (mean) of U under the null hypothesis, σ_U^2 represents the variance of U under the null hypothesis (assuming no tied ranks), and Z is the standardized statistic. As the smaller sample size $\min(n_1, n_2) \to \infty$, the distribution of Z converges in distribution to a standard normal distribution $\mathcal{N}(0,1)$ by the central limit theorem, enabling the use of standard normal critical values for hypothesis testing. We employed a two-sided test to detect differences in either direction, testing whether |Z| exceeds the critical value $z_{\alpha/2}$ for significance level α .

2.4.2 Wilcoxon Rank-Sum Test

The Wilcoxon rank-sum test (Wilcoxon, 1945) is mathematically equivalent to the Mann-Whitney U test but formulated in terms of the sum of ranks rather than pairwise comparisons. The test statistic is defined as:

$$W = R_1 = \sum_{i=1}^{n_1} r_i, \tag{16}$$

where W is the Wilcoxon rank-sum statistic, R_1 is the sum of all ranks assigned to the first sample (LGM), and r_i denotes the rank of the i-th observation X_i in the combined sample of size $N=n_1+n_2$ observations pooled from both groups and ranked from 1 (smallest) to N (largest). The mathematical relationship between the Mann-Whitney U statistic and the Wilcoxon rank-sum statistic W is given by $U=W-n_1(n_1+1)/2$, which ensures that the two tests are algebraically equivalent and will always yield identical p-values and conclusions. Under the null hypothesis $H_0:F=G$, the expected value and variance of W are:

$$Z_W = \frac{W - \mathbb{E}[W]}{\sqrt{\text{Var}(W)}}, \quad \mathbb{E}[W] = \frac{n_1(n_1 + n_2 + 1)}{2}, \quad \text{Var}(W) = \frac{n_1n_2(n_1 + n_2 + 1)}{12}, \tag{17}$$

where $\mathbb{E}[W]$ denotes the expected value (mean) of the rank sum W when both samples are drawn from identical distributions, Var(W) denotes the variance of W under the null hypothesis, and Z_W is the standardized test statistic that asymptotically follows a standard normal distribution for large samples.

2.4.3 Kruskal-Wallis H Test

314

322

324

325

326

329

331

332

334

335

336

338

The Kruskal-Wallis test (Kruskal and Wallis, 1952) provides a nonparametric generalization of the oneway analysis of variance (ANOVA) that can accommodate $k \ge 2$ independent groups. Although designed for multiple groups, it reduces to a test equivalent to the Mann-Whitney/Wilcoxon tests when applied to k = 2 groups. The test is based on rank-based analysis of variance and detects differences in the central tendency across groups. For k = 2 groups (LGM and LH), the test statistic is:

$$H = \frac{12}{N(N+1)} \sum_{i=1}^{k} \frac{R_j^2}{n_j} - 3(N+1), \tag{18}$$

where $N = n_1 + n_2$ is the total sample size combining both groups, k = 2 is the number of groups being compared, $R_j = \sum_{i=1}^{n_j} r_{ji}$ represents the sum of ranks for group j (where r_{ji} denotes the rank of the i-th observation in group j within the combined sample), and n_j is the sample size of group j. The constants 12 and 3 are chosen such that under the null hypothesis $H_0: F = G$ (all groups have identical distributions), the statistic H asymptotically follows a chi-squared distribution with k-1 degrees of freedom: $H \sim \chi_{k-1}^2$ as $n_j \to \infty$ for all j.

When tied ranks are present in the data (multiple observations with identical values), the test statistic must be corrected to account for the reduced variance in the rank sums. The tie-corrected statistic is:

$$H_c = \frac{H}{1 - \frac{\sum_{i=1}^{g} (t_i^3 - t_i)}{N^3 - N}},\tag{19}$$

where g denotes the number of distinct groups of tied values in the pooled sample, t_i represents the number of observations tied at the i-th tied value (the size of the i-th tied group), and the denominator correction factor accounts for the reduction in variance caused by ties. The correction increases the test statistic H to maintain appropriate Type I error rates when ties are present, as ties reduce the variability in possible rank configurations.

2.4.4 Mood's Median Test

Mood's median test (Mood, 1954) provides an extremely robust nonparametric test for comparing the central tendencies of two or more groups based on the median rather than means or ranks. The test is particularly resistant to outliers and extreme values because it only considers whether observations fall above or below the grand median, discarding information about the magnitude of deviations. The procedure constructs a 2×2 contingency table based on the grand median M of the pooled sample, defined as the middle value (or average of two middle values) when all $N = n_1 + n_2$ observations are arranged in order. The contingency table records the number of observations from each group falling above and below this grand median:

$$\begin{array}{c|cccc}
 & X_i \leq M & X_i > M \\
\hline
 & LGM & a & b \\
 & LH & c & d
\end{array} \tag{20}$$

where a denotes the number of LGM observations less than or equal to the grand median, b denotes the number of LGM observations greater than the grand median, c denotes the number of LH observations less than or equal to the grand median, and d denotes the number of LH observations greater than the grand median. Note that by definition, $a + b = n_1$, $c + d = n_2$, and a + b + c + d = N.

The test statistic follows Pearson's chi-squared form for testing independence in a 2×2 contingency table:

$$\chi^2 = \frac{N(ad - bc)^2}{(a+b)(c+d)(a+c)(b+d)},\tag{21}$$

where N = a + b + c + d is the total sample size, ad - bc represents the cross-product difference (a measure of association in the 2×2 table), and the denominator contains the product of the four marginal totals. Under the null hypothesis that the medians of the two populations are equal, H_0 : median(F) =median(G), the test statistic asymptotically follows a chi-squared distribution with one degree of freedom: $\chi^2 \sim \chi_1^2$ as $N \to \infty$. The test is particularly useful when extreme observations or outliers may unduly influence rank-based tests.

2.4.5 Kolmogorov-Smirnov Two-Sample Test

344

345

346

351

354

356

358

360

365

367

372

374

375

376

378

The two-sample Kolmogorov-Smirnov test (Smirnov, 1948) extends the one-sample KS test to the two-sample setting, providing a nonparametric test for the equality of two continuous probability distributions. Unlike tests focused on location or scale, the KS test is sensitive to any differences between distributions, including differences in location (central tendency), dispersion (spread), and shape (skewness, kurtosis, multimodality). The test quantifies the maximum absolute vertical distance between the two empirical cumulative distribution functions:

$$D_{n_1,n_2} = \sup_{x \in \mathbb{R}} |F_{n_1}(x) - G_{n_2}(x)|, \tag{22}$$

$$F_{n_1}(x) = \frac{1}{n_1} \sum_{i=1}^{n_1} \mathbb{I}(X_i \le x), \quad G_{n_2}(x) = \frac{1}{n_2} \sum_{j=1}^{n_2} \mathbb{I}(Y_j \le x), \tag{23}$$

where $D_{n_1,n_2} \in [0,1]$ is the KS test statistic representing the supremum (maximum) deviation between the two empirical CDFs, $F_{n_1}(x)$ is the empirical CDF of the LGM sample (the proportion of LGM observations less than or equal to x), $G_{n_2}(x)$ is the empirical CDF of the LH sample (the proportion of LH observations less than or equal to x), and $\mathbb{I}(X_i \leq x)$ is the indicator function equal to 1 if observation X_i is less than or equal to the evaluation point x and 0 otherwise. The supremum is taken over all possible values $x \in \mathbb{R}$, meaning we find the x value where the vertical distance between the two step functions is largest.

Under the null hypothesis of distributional equality $H_0: F = G$, the asymptotic distribution of the appropriately scaled KS statistic is given by the Kolmogorov distribution:

$$\lim_{n_1, n_2 \to \infty} P\left(\sqrt{\frac{n_1 n_2}{n_1 + n_2}} D_{n_1, n_2} \le z\right) = 1 - 2\sum_{k=1}^{\infty} (-1)^{k-1} e^{-2k^2 z^2},\tag{24}$$

where the scaling factor $\sqrt{n_1n_2/(n_1+n_2)}$ is the harmonic mean of the sample sizes and ensures convergence to the limiting distribution, z>0 is the argument of the cumulative distribution function, and the infinite series $\sum_{k=1}^{\infty} (-1)^{k-1}e^{-2k^2z^2}$ defines the Kolmogorov distribution. This limiting distribution is valid when both n_1 and n_2 tend to infinity, and it provides the theoretical basis for computing asymptotic p-values for the test. The two-sample KS test is distribution-free, meaning its null distribution does not depend on the specific form of F and G as long as they are continuous.

Epps-Singleton Test The Epps-Singleton test (Epps and Singleton, 1986) provides a powerful omnibus test for distributional equality based on the empirical characteristic function rather than the empirical distribution function. The characteristic function is the Fourier transform of the probability density function and uniquely characterizes the distribution. By comparing characteristic functions rather than

CDFs, the Epps-Singleton test can detect differences in all aspects of the distribution simultaneously with good power properties. The test statistic is defined as:

$$W = \frac{n_1 n_2}{n_1 + n_2} \int_{-\infty}^{\infty} \left| \hat{\phi}_{n_1}(t) - \hat{\phi}_{n_2}(t) \right|^2 w(t) dt, \tag{25}$$

where $W \geq 0$ is the test statistic measuring the weighted integrated squared difference between empirical characteristic functions, n_1 and n_2 are the sample sizes, $\hat{\phi}_n(t) = n^{-1} \sum_{j=1}^n e^{itX_j}$ is the empirical characteristic function of sample **X** evaluated at frequency $t \in \mathbb{R}$ (where $i = \sqrt{-1}$ is the imaginary unit and $e^{itX_j} = \cos(tX_j) + i\sin(tX_j)$ by Euler's formula), $\hat{\phi}_{n_1}(t)$ and $\hat{\phi}_{n_2}(t)$ are the empirical characteristic functions for the LGM and LH samples respectively, $|\cdot|$ denotes the complex modulus (absolute value), and w(t) is a suitable weight function that ensures integrability and places emphasis on frequencies where the characteristic functions are most reliably estimated.

In practice, the integral in Equation 25 is approximated by a discrete sum over a finite set of frequencies. The computational form uses discrete approximation:

$$W_n = \sum_{k=1}^{n_1 + n_2 - 1} w_k \left| \hat{\phi}_{n_1}(t_k) - \hat{\phi}_{n_2}(t_k) \right|^2, \tag{26}$$

where W_n is the numerically computed test statistic, the sum runs over $n_1 + n_2 - 1$ evaluation frequencies, t_k for $k = 1, ..., n_1 + n_2 - 1$ are the discrete frequencies at which the empirical characteristic functions are evaluated (typically chosen based on the data scale and spacing), and w_k are the corresponding discrete weights that approximate the continuous weight function w(t). The specific choices of t_k and w_k are determined by the implementation algorithm. Under the null hypothesis $H_0: F = G$, the statistic W (or W_n) has a known asymptotic distribution that can be approximated through resampling methods or asymptotic theory, enabling computation of p-values. The test is particularly powerful for detecting shape differences that may be subtle in the CDF but pronounced in the characteristic function domain.

2.4.6 Effect Size: Cliff's Delta

385

390

394

397

400

409

411

412

414

415

416

418

To quantify the magnitude of distributional differences between epochs independent of sample size and statistical significance, we computed Cliff's δ (Cliff) [1993], a nonparametric effect size measure analogous to the probability of superiority in receiver operating characteristic analysis. Unlike standardized mean differences (such as Cohen's d), Cliff's δ makes no assumptions about the distributions and is robust to outliers. The measure is defined as:

$$\delta = \frac{1}{n_1 n_2} \sum_{i=1}^{n_1} \sum_{i=1}^{n_2} \operatorname{sgn}(X_i - Y_j) = \frac{\#(X_i > Y_j) - \#(X_i < Y_j)}{n_1 n_2},$$
(27)

where $\delta \in [-1,1]$ is Cliff's delta effect size, $\operatorname{sgn}(z) = \mathbb{I}(z>0) - \mathbb{I}(z<0)$ is the sign function that equals +1 when z>0, -1 when z<0, and 0 when z=0, $\#(X_i>Y_j)$ denotes the number of pairs where the LGM observation exceeds the LH observation, $\#(X_i< Y_j)$ denotes the number of pairs where the LGM observation is less than the LH observation, and the denominator n_1n_2 represents the total number of possible pairwise comparisons. The effect size $\delta=1$ indicates complete separation with all LGM values exceeding all LH values, $\delta=-1$ indicates complete separation in the opposite direction, and $\delta=0$ indicates no systematic difference (equal probability of $X_i>Y_j$ and $X_i< Y_j$).

Interpretation of effect size magnitude follows the guidelines established by Romano et al. (2006): $|\delta| < 0.147$ indicates a negligible effect (little practical difference between distributions), $0.147 \le |\delta| < 0.330$ indicates a small effect, $0.330 \le |\delta| < 0.474$ indicates a medium effect (moderate practical importance), and $|\delta| \ge 0.474$ indicates a large effect (substantial practical significance). These thresholds provide context for interpreting the scientific importance of statistically significant differences.

All hypothesis tests were implemented using established functions from the SciPy library (Virtanen et al., 2020): scipy.stats.mannwhitneyu for the Mann-Whitney U test, scipy.stats.ranksums for the Wilcoxon rank-sum test, scipy.stats.kruskal for the Kruskal-Wallis H test,

scipy.stats.median_test for Mood's median test, scipy.stats.ks_2samp for the two-sample Kolmogorov-Smirnov test, and scipy.stats.epps_singleton_2samp for the Epps_Singleton test. For each pairwise comparison between LGM and LH distributions, statistical significance was evaluated at the conventional threshold $\alpha=0.05$ (corresponding to a 95% confidence level). Following a conservative approach to minimize false positive conclusions, we defined strong evidence for distributional differences as present when $\geq 70\%$ of the seven tests reached statistical significance (i.e., when at least five out of seven tests yielded p < 0.05), ensuring robust detection of genuine distributional shifts while accounting for potential variations in test power and sensitivity.

2.5 Information-Theoretic Complexity Measures

We quantified the complexity, regularity, and variability structure of paleoclimate distributions using complementary information-theoretic and statistical dispersion measures (Cover and Thomas) [2006].

These metrics provide dimensionless, scale-independent characterizations of distributional properties that enable cross-variable and cross-epoch comparisons despite differences in measurement units and ranges.

433 2.5.1 Shannon Entropy

For discretized probability distributions, Shannon entropy (Shannon, 1948) provides a fundamental measure of information content, uncertainty, and distributional complexity. The entropy quantifies the average information required to describe a randomly selected observation from the distribution, with higher entropy indicating greater uncertainty and more uniform probability mass distribution. For a discrete probability mass function $\mathbf{p} = \{p_i\}_{i=1}^m$ obtained through histogram binning with m bins, where $p_i \geq 0$ represents the probability mass (relative frequency) in bin i and $\sum_{i=1}^m p_i = 1$, Shannon entropy is defined as:

$$H(\mathbf{p}) = -\sum_{i=1}^{m} p_i \log_2 p_i, \tag{28}$$

where $H(\mathbf{p}) \ge 0$ is measured in bits (when using logarithm base 2), the summation runs over all m bins, and we adopt the standard convention $0 \log 0 = 0$ to handle empty bins where $p_i = 0$ (based on the limit $\lim_{x\to 0^+} x \log x = 0$). The entropy achieves its minimum value H = 0 bits for a deterministic distribution (all probability mass concentrated in a single bin) and its maximum value $H = \log_2 m$ bits for a uniform distribution (equal probability mass $p_i = 1/m$ in all bins).

For a continuous random variable X with probability density function f(x), the analogous concept is differential entropy, defined as $h(X) = -\int_{-\infty}^{\infty} f(x) \log_2 f(x) dx$, which we approximate through histogram binning of the continuous data. We employed m = 50 bins with equal width spanning the data range to discretize each continuous distribution. The probability mass in each bin was computed via density normalization: $p_i = h_i / \sum_{j=1}^m h_j$, where h_i denotes the count (number of observations) falling in bin i and the denominator ensures $\sum_{i=1}^m p_i = 1$. Higher entropy values indicate distributions with greater complexity, more spread, or more uniform probability distribution across the variable's range, while lower entropy indicates distributions with probability mass concentrated in fewer bins.

2.5.2 Approximate Entropy

Approximate entropy (ApEn) (Pincus, 1991) provides a complementary measure of regularity and predictability in sequential data, originally developed for physiological time series but applicable to any ordered sequence of observations. ApEn quantifies the logarithmic likelihood that sequences of patterns that are close to each other will remain close when one additional observation is added. Lower ApEn values indicate greater regularity, predictability, and deterministic structure in the sequence, while higher values indicate more complex, irregular, or random behavior.

For a sequence $\mathbf{u} = \{u(i)\}_{i=1}^N$ of N observations (where i indexes the position in the sequence), ApEn is computed using an embedding dimension $m \in \mathbb{N}$ (typically m = 2) and a tolerance threshold $r \in \mathbb{R}_+$ that defines closeness:

$$ApEn(m,r,N) = \Phi^{m}(r) - \Phi^{m+1}(r), \tag{29}$$

$$\Phi^{m}(r) = \frac{1}{N - m + 1} \sum_{i=1}^{N - m + 1} \log C_{i}^{m}(r), \tag{30}$$

$$C_i^m(r) = \frac{\#\{j \in [1, N - m + 1] : d[\mathbf{x}^m(i), \mathbf{x}^m(j)] \le r\}}{N - m + 1},$$
(31)

where ApEn(m,r,N) > 0 is the ApEn value (with units depending on the logarithm base), $\Phi^m(r)$ represents the average logarithm of the correlation integral at embedding dimension m, $C_i^m(r)$ is the correlation integral measuring the fraction of m-dimensional patterns similar to the pattern starting at position i, $\mathbf{x}^m(i) = [u(i), u(i+1), \dots, u(i+m-1)]^{\top} \in \mathbb{R}^m$ denotes the m-dimensional delay embedding vector (a vector formed by m consecutive observations starting at position i), $d[\mathbf{a}, \mathbf{b}] = \max_{k=1,\dots,m} |a_k - b_k|$ is the Chebyshev distance (also called maximum or L^{∞} distance), which measures the maximum absolute difference across all m components between vectors **a** and **b**, $\#\{\cdot\}$ denotes the cardinality (count) of the set, and [1, N-m+1] denotes the integer interval of valid starting positions for m-dimensional patterns. The tolerance parameter r determines how similar two patterns must be to be considered "close."

Following standard guidelines (Pincus, 1991), we employed m=2 for the embedding dimension and $r = 0.2 \times \mathrm{SD}(X)$ for the tolerance, where $\mathrm{SD}(X) = \sqrt{n^{-1} \sum_{i=1}^{n} (x_i - \bar{x})^2}$ is the standard deviation of the sequence **u**. The choice $r = 0.2 \times \mathrm{SD}(X)$ provides a scale-independent tolerance that adapts to the variability of each dataset. Lower ApEn values (approaching 0) indicate highly regular, predictable sequences where similar patterns consistently repeat, while higher ApEn values indicate irregular, complex sequences where patterns are less predictable and the addition of one observation substantially changes the pattern structure.

2.6 Normalized Variability Measures

465

466

468

470

471

472

473

474 475

476

477

479

480

481

482

483

487

488

489

490

491

492

493

495

496

497

499

To enable direct comparison of variability across variables measured in different units and with different central tendencies (e.g., temperature in °C, salinity in PSU, isotope ratios in ‰), we computed three complementary scale-invariant dispersion metrics. These dimensionless measures normalize absolute dispersion by measures of central tendency, providing relative variability metrics:

$$CV(X) = \frac{\hat{\sigma}_X}{\bar{X}},\tag{32}$$

$$RSD(X) = \frac{IQR(X)}{\text{median}(X)},$$

$$NR(X) = \frac{\max(X) - \min(X)}{\text{median}(X)},$$
(33)

$$NR(X) = \frac{\max(X) - \min(X)}{\operatorname{median}(X)},$$
(34)

where CV(X) denotes the coefficient of variation (a dimensionless ratio of standard deviation to mean), $\hat{\sigma}_X = \sqrt{n^{-1} \sum_{i=1}^n (x_i - \bar{X})^2}$ is the sample standard deviation of variable $X, \bar{X} = n^{-1} \sum_{i=1}^n x_i$ is the sample mean, RSD(X) denotes the robust spread dispersion metric based on the interquartile range relative to the median, $IQR(X) = Q_3(X) - Q_1(X)$ is the interquartile range (the difference between the third quartile Q_3 and first quartile Q_1 , encompassing the middle 50% of the data), median(X) is the sample median (the 50th percentile or middle value when data are ordered), NR(X) denotes the normalized range, and $\max(X) - \min(X)$ is the sample range (the difference between maximum and minimum values).

The coefficient of variation CV is particularly useful for comparing the relative variability of variables with different means, but it can be sensitive to outliers and is undefined or unstable when the mean is near zero. The robust spread dispersion RSD provides a more outlier-resistant alternative based on quantiles rather than moments, measuring the relative spread of the central 50% of the data. The normalized range NR quantifies the full spread of the data relative to the central tendency but is highly sensitive to extreme values. Together, these three metrics provide complementary perspectives on distributional variability: CV for parametric mean-based relative variability, RSD for robust central-region relative variability, and NR for total range relative variability. All three ratios are dimensionless (unitless), enabling direct comparison across variables with different measurement scales.

Entropy calculations were implemented using custom Python algorithms following the specifications of Pincus (1991) for ApEn computation, with Shannon entropy computed using the scipy.stats.entropy function from the SciPy library (Virtanen et al.), 2020), which handles the discrete probability mass function and applies appropriate conventions for zero probabilities. All statistical computations, array operations, and data manipulations employed NumPy (Harris et al.), 2020) for efficient numerical computing, Pandas (McKinney, 2010) for tabular data structures and statistical functions, and xarray (Hoyer and Hamman, 2017) for labeled multi-dimensional array operations on gridded paleoclimate datasets.

3 RESULTS

All three oceanographic variables exhibited strongly non-normal distributions in both epochs, with all five normality tests (Shapiro-Wilk, Anderson-Darling, Kolmogorov-Smirnov, D'Agostino-Pearson, and Jarque-Bera) rejecting normality at p < 0.001 for both LGM and LH populations. Figure [I] displays the probability density distributions and statistical dispersion for all three variables. SST during the LGM exhibited a mean of 25.639°C (median: 25.708°C, SD: 0.887°C), substantially lower than the LH mean of 28.427°C (median: 28.526°C, SD: 0.583°C), yielding a mean cooling of 2.788°C. The LGM SST distribution showed greater absolute spread (range: 6.183°C) compared to LH (range: 3.787°C), but lower relative variability (coefficient of variation: 0.035 vs 0.021). SSS demonstrated a reversed pattern, with LGM values (mean: 33.777 PSU, median: 34.012 PSU, SD: 0.668 PSU) exceeding LH values (mean: 32.893 PSU, median: 33.517 PSU, SD: 1.664 PSU) by 0.884 PSU. The LH SSS distribution exhibited substantially greater variability, with a range of 11.389 PSU compared to the LGM range of 4.164 PSU. For $\delta^{18}O_{sw}$, the LGM showed uniformly enriched values (mean: 0.803% $_{o}$, median: 0.842% $_{o}$, SD: 0.208% $_{o}$) relative to LH (mean: -0.198% $_{o}$, median: -0.033% $_{o}$, SD: 0.439% $_{o}$), with a mean difference of 1.001% $_{o}$. The LGM $\delta^{18}O_{sw}$ distribution was markedly more constrained (range: 1.320% $_{o}$) than LH (range: 3.015% $_{o}$).

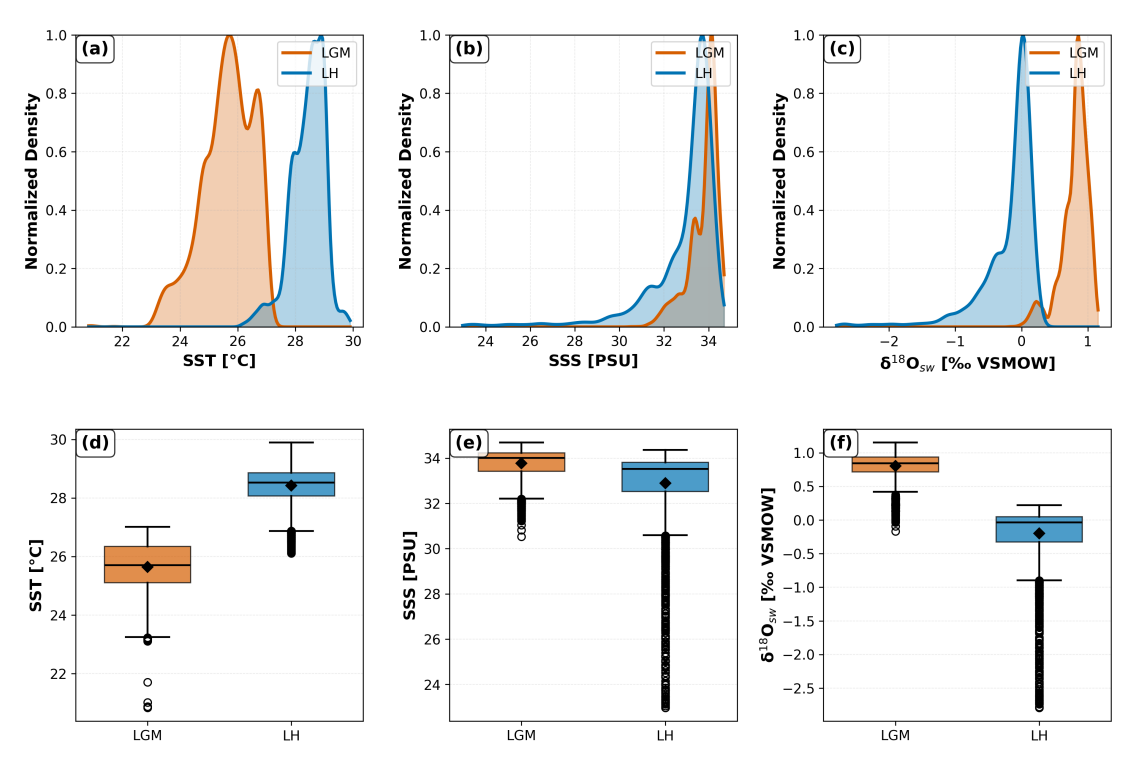


Figure 1. Probability density distributions and statistical dispersion of oceanographic variables during the LGM (orange) and LH (blue). (a-c) Kernel density estimates normalized to unity maximum for SST, SSS, and $\delta^{18}O_{sw}$, with shaded regions indicating the probability density. (d-f) Box-and-whisker plots showing median (horizontal line), mean (diamond), interquartile range (box), and full data range excluding outliers (whiskers) for each variable. Black circles indicate outlier values beyond 1.5 times the interquartile range from the box boundaries. LGM exhibits cooler SST, higher SSS, and enriched $\delta^{18}O_{sw}$ relative to LH, with distinct distributional characteristics for each variable.

524

525

526 527

528

529

530

531

532

534

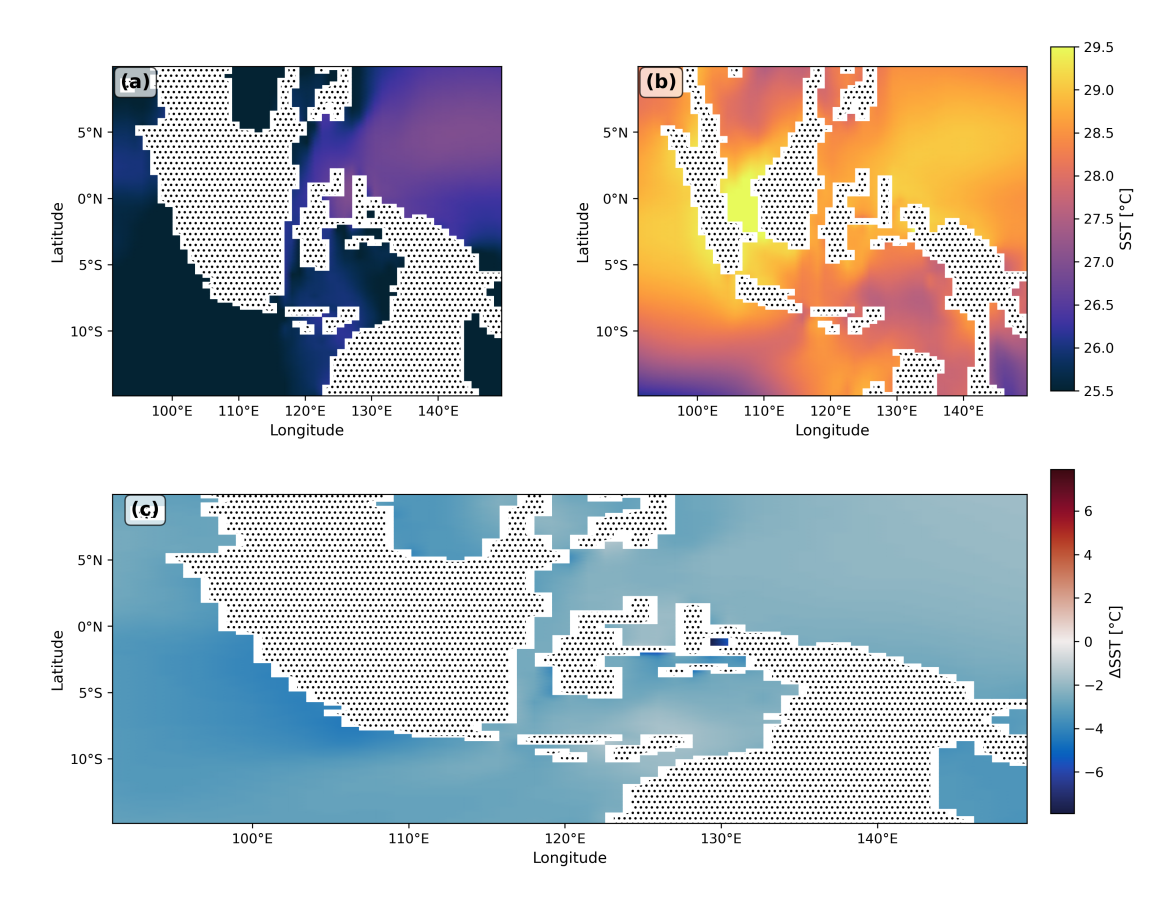


Figure 2. Spatial distribution of SST across the Indo-Pacific warm pool. (a) LGN SST field showing temperatures between 25.5°C and 29.5°C with cooler conditions in the eastern warm pool. (b) LH SST field displaying uniformly warm temperatures between 26.0°C and 29.5°C across the basin. (c) LGM minus LH anomaly field revealing basin-wide cooling of 2-8°C, with strongest cooling in the central and eastern warm pool regions. Stippling indicates land areas. Color scales are optimized to highlight spatial gradients within each epoch and in the anomaly field.

SSS spatial patterns demonstrated substantial heterogeneity between epochs (Figure 3). During the LGM, salinity ranged from 30.532 PSU to 34.696 PSU, with the freshest waters at 5.80°N, 109.06°E and most saline waters at 0.67°S, 149.56°E. The LH exhibited a broader salinity range (22.968-34.357 PSU), with extreme freshening at 2.27°S, 107.94°E and highest salinity at 14.87°S, 146.19°E. The anomaly field revealed complex spatial structure, with positive anomalies (LGM saltier) dominating most of the domain but negative anomalies in localized regions. Anomaly magnitudes ranged from -0.831 PSU to +4.114 PSU, with the maximum positive anomaly occurring at 6.01°S, 105.69°E.

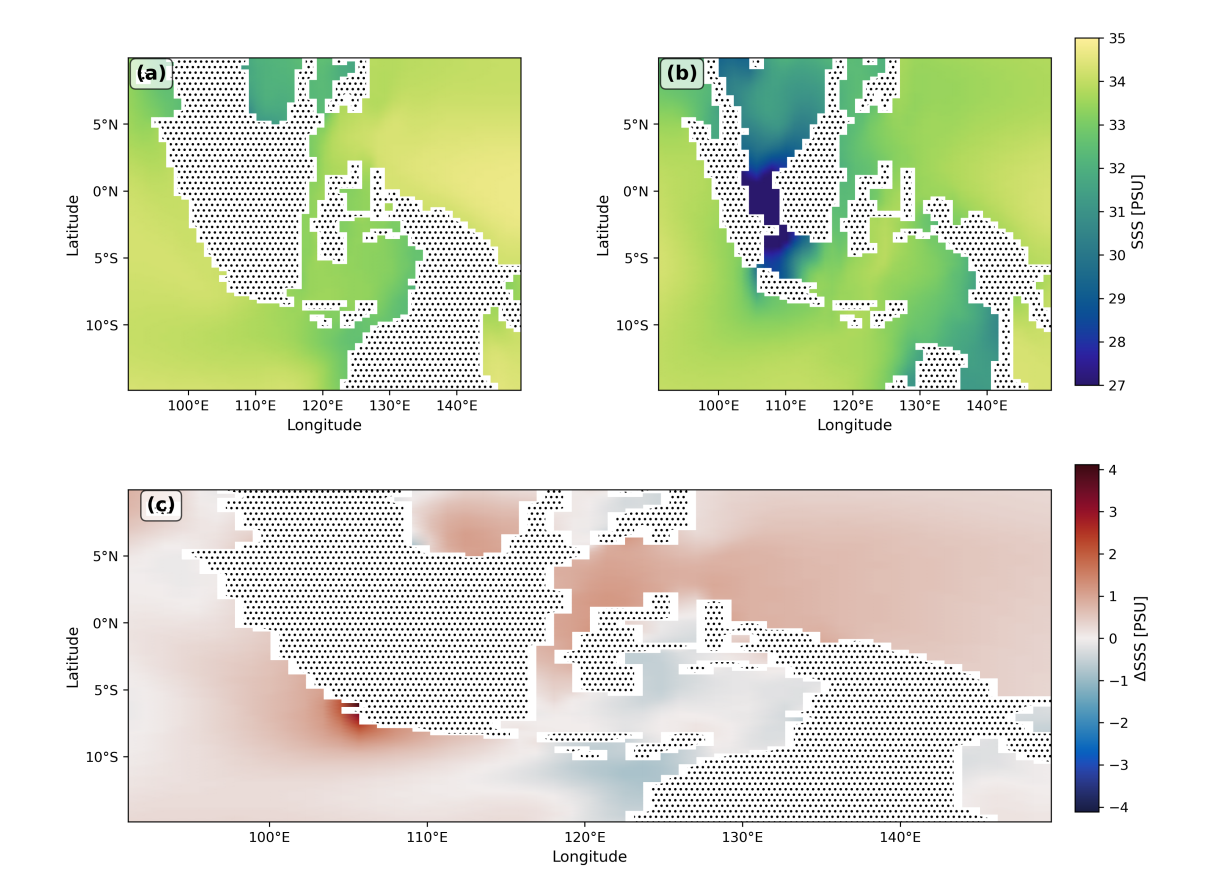


Figure 3. Spatial distribution of SSS across the Indo-Pacific warm pool. (a) LGM SSS field showing relatively uniform salinity between 27 and 35 PSU with fresher conditions in northern regions. (b) LH SSS field displaying strong spatial gradients with pronounced freshening in the Java Sea and eastern Indonesian archipelago (27-34 PSU) and elevated salinity in the southeastern warm pool. (c) LGM minus LH anomaly field showing predominantly positive values (LGM saltier) across most of the domain, with localized negative anomalies (LGM fresher) reaching -4 PSU in limited regions. Stippled regions indicate land masses. The LH exhibits substantially greater spatial variability than the LGM.

The $\delta^{18}O_{sw}$ field showed systematic enrichment during the LGM throughout the entire domain (Figure 4). LGM values ranged from -0.166‰ to 1.155‰, with depletion at 5.80°N, 109.06°E and enrichment at 14.87°S, 146.19°E. LH values were substantially more depleted, spanning -2.792‰ to 0.223‰, with extrema at 2.27°S, 107.94°E and 14.87°S, 146.19°E. The anomaly field exhibited exclusively positive values, ranging from 0.505‰ to 1.730‰, indicating ubiquitous LGM enrichment. The spatial pattern of enrichment was relatively uniform, with maximum anomalies occurring at 6.01°S, 105.69°E and minimum anomalies at 5.80°N, 109.06°E.

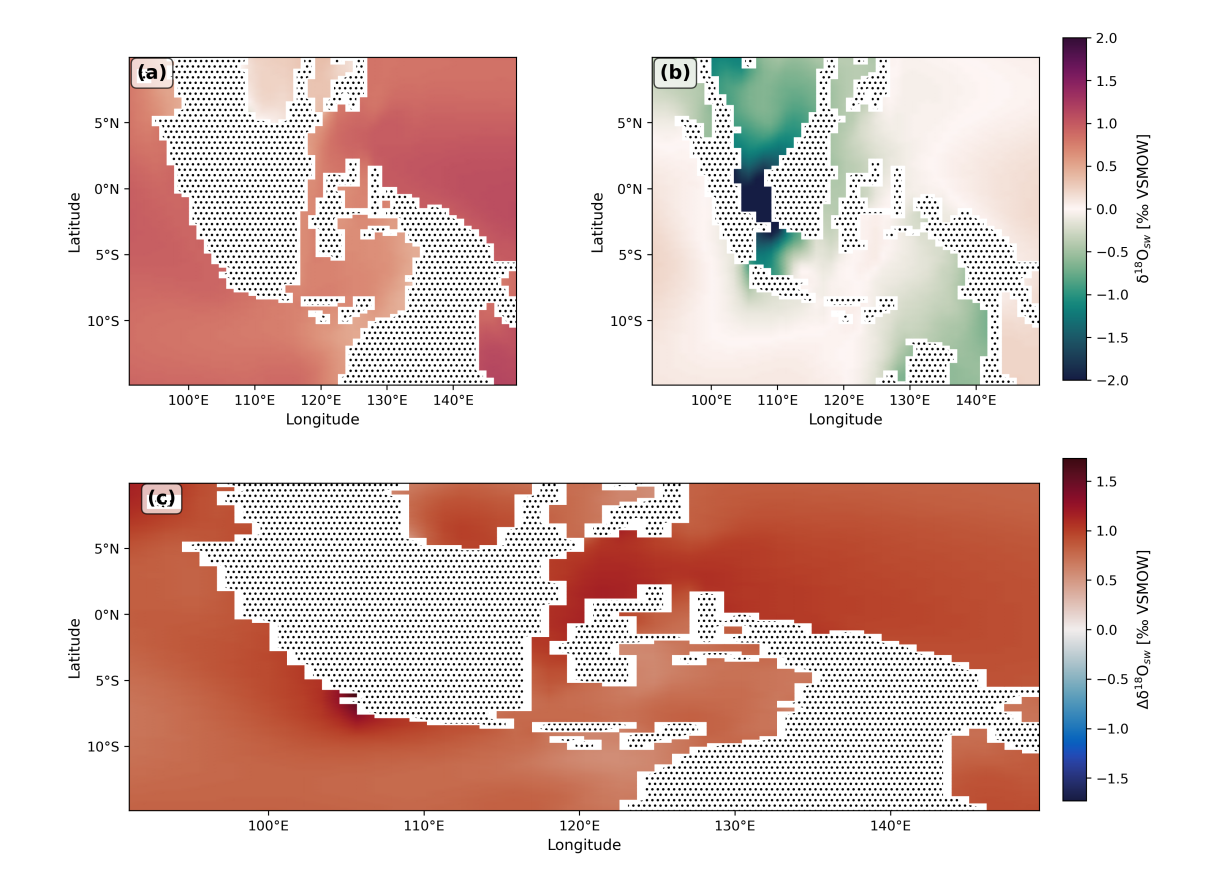


Figure 4. Spatial distribution of $\delta^{18}O_{sw}$ across the Indo-Pacific warm pool. (a) LGM $\delta^{18}O_{sw}$ field showing enriched values between 0.0% and 2.0% VSMOW with relatively uniform spatial distribution. (b) LH $\delta^{18}O_{sw}$ field displaying substantially more depleted values between -2.0% and 0.0% VSMOW, with strong depletion in the Java Sea and fresher regions. (c) LGM minus LH anomaly field revealing uniformly positive anomalies (LGM enriched) throughout the domain, ranging from 0.5% to 1.7% VSMOW. Stippled regions indicate land masses. The consistent positive anomaly reflects both global ice volume effects and regional hydrological changes.

Table $\[\]$ summarizes the descriptive statistics for all three variables across both epochs. The comprehensive nonparametric statistical testing revealed highly significant differences between LGM and LH distributions for all variables. All six nonparametric tests (Mann-Whitney U, Wilcoxon rank-sum, Kruskal-Wallis H, Mood's median, Kolmogorov-Smirnov two-sample, and Epps-Singleton) yielded p < 0.001 for SST, SSS, and $\delta^{18}O_{sw}$, indicating strong evidence for distributional differences. Effect size quantification via Cliff's delta revealed large effects for SST ($\delta = -0.993$) and $\delta^{18}O_{sw}$ ($\delta = 0.994$), with a medium effect for SSS ($\delta = 0.469$). The direction of effects indicated that LGM exhibited lower SST values, higher SSS values, and higher $\delta^{18}O_{sw}$ values relative to LH.

Table 1. Descriptive statistics for oceanographic variables during the LGM and LH across the Indo-Pacific warm pool domain (n = 1,872 grid points per epoch).

Variable	Epoch	Mean	Median	SD	Min	Max
	LGM	25.639	25.708	0.887	20.832	27.015
SST [°C]	LH	28.427	28.526	0.583	26.112	29.898
	Δ (LGM-LH)	-2.788	-2.707	0.615	-7.910	-1.354
	LGM	33.777	34.012	0.668	30.532	34.696
SSS [PSU]	LH	32.893	33.517	1.664	22.968	34.357
	Δ (LGM-LH)	0.884	0.494	1.331	-0.831	4.114
	LGM	0.803	0.842	0.208	-0.166	1.155
$\delta^{18}\mathrm{O}_\mathrm{sw}$ [% $_{o}$ VSMOW]	LH	-0.198	-0.033	0.439	-2.792	0.223
	Δ (LGM-LH)	1.001	0.875	0.356	0.505	1.730

Information-theoretic complexity analysis quantified distributional structure differences between epochs (Table 2). Shannon entropy indicated that LH SST exhibited greater distributional complexity (3.350 bits) than LGM SST (3.248 bits), while LGM exhibited higher complexity for both SSS (3.215 vs 2.719 bits) and $\delta^{18}O_{sw}$ (3.254 vs 2.795 bits). ApEn measures revealed that LGM SST displayed greater regularity (ApEn = 0.650) compared to LH (ApEn = 0.742), while LH showed greater regularity for SSS (ApEn = 0.486 vs 0.545) and $\delta^{18}O_{sw}$ (ApEn = 0.504 vs 0.526). Coefficient of variation values demonstrated that LGM exhibited higher relative variability for SST (0.035 vs 0.021) and $\delta^{18}O_{sw}$ (0.258 vs -2.216), while LH showed substantially greater relative variability for SSS (0.051 vs 0.020).

Table 2. Information-theoretic complexity measures and variability metrics for oceanographic variables during the LGM and LH.

	Shannon Entropy [bits]			Approximate Entropy		Coefficient of Variation	
Variable	LGM	LH	Δ	LGM	LH	LGM	LH
SST	3.248	3.350	-0.102	0.650	0.742	0.035	0.021
SSS	3.215	2.719	0.497	0.545	0.486	0.020	0.051
$\delta^{18}\mathrm{O}_\mathrm{sw}$	3.254	2.795	0.460	0.526	0.504	0.258	-2.216

4 DISCUSSION

Our statistical characterization reveals a fundamental reorganization of the IMC's oceanography between the LGM and the LH. The robust, non-parametric tests and large effect sizes (Cliff's δ) for SST, SSS, and $\delta^{18}O_{sw}$ confirm that these are not merely shifts in the mean state, but represent profound changes in the underlying distributional properties of the oceanographic fields. The LGM was characterized by a cooler, saltier, and more isotopically enriched ocean with reduced spatial heterogeneity, while the LH presents a warmer, fresher (in key regions), and markedly more variable regime. These changes can be interpreted through the interplay of global forcings and regional dynamics, including ice volume, sea level, and the intensity and vertical structure of the ITF.

The \sim 2.8°C of glacial cooling and the \sim 1.0% enrichment of $\delta^{18}O_{sw}$ are consistent with global-scale LGM boundary conditions, primarily the expansion of continental ice sheets (Clark et al.) [2009]. Our findings align closely with proxy reconstructions from the Makassar Strait, which show LGM SSTs were \sim 2–3°C cooler and SSS was 0.82–1.13 PSU higher than in the LH (Larasati et al.) [2024]. The spatial pattern of SST change, with strongest cooling in the eastern warm pool, points to regional atmospheric and oceanic controls. This pattern is suggestive of a strengthened zonal SST gradient and enhanced easterly trade winds during the LGM, which could have intensified upwelling in the eastern IMC (DiNezio et al.) [2018].

The drastically reduced spatial variability of both SSS and $\delta^{18}O_{sw}$ during the LGM indicates a weakening of the strong hydrological gradients that define the modern IMC. This implies a significant reduction in the freshwater inputs that today create pronounced low-salinity plumes. A primary mechanism for this change was the \sim 120 meter lower sea level, which exposed the Sunda and Sahul continental

shelves (Hanebuth et al., 2009), altering coastline geometry and displacing the mouths of major rivers (Hendrizan et al., 2021). This is corroborated by proxy evidence showing a larger south-north SSS gradient in the Makassar Strait during the LGM (23.2–24.2 ka), attributed to reduced freshwater runoff from Kalimantan into the southern strait (Larasati et al., 2024).

The co-occurrence of higher glacial SSS and enriched $\delta^{18}O_{sw}$ suggests a regional hydrological shift towards drier conditions, supported by paleoclimatic records from Borneo, Sulawesi, and Java (Konecky et al., 2016; Wicaksono et al., 2017). This aridity has been linked to a weakened Asian monsoon and a southward shift of the Intertropical Convergence Zone (ITCZ) (Schröder et al., 2018; Hendrizan et al., 2021).

The observed oceanographic changes are inextricably linked to the intensity and vertical structure of the Indonesian Throughflow (ITF). Our results are consistent with a weaker glacial ITF, particularly in its surface layers. A weaker ITF would have reduced the inflow of fresh, warm water from the western Pacific, allowing local evaporation to dominate the surface salinity budget (Gordon et al.) [2012]. This is supported by proxy data from the Makassar Strait, where a larger south-north SST gradient during the LGM (e.g., 0.5–1°C around 23-24 ka) is interpreted as a direct indicator of weakened surface ITF intensity (Larasati et al.) [2024]; [Fan et al.] [2018]). Model simulations from the CCSM4 model further illuminate the complex spatial pattern of this change, indicating that while the ITF was generally weaker during the LGM, its strength relative to the Pre-Industrial (PI) period varied across pathways. The model shows a more robust ITF in the eastern pathway (Banda Sea) during the LGM compared to the PI, suggesting a redistribution of flow within the archipelago under glacial boundary conditions (Rachmayani et al.) [2025].

The analysis of thermocline water temperature (TWT) gradients provides critical insight into the vertical structure of the ITF. The predominantly negative S-N TWT gradients in the Makassar Strait during the LGM indicate cooler southern waters, consistent with reduced advection of warm Pacific waters and a shallower, more stratified thermocline (Rachmayani et al., 2025; Xu et al., 2008). This enhanced stratification and reduced vertical mixing would have further contributed to the preservation of the strong surface gradients observed in the proxy records (Larasati et al., 2024). The weaker ITF has been linked to a persistent, "El Niño-like" mean state in the Pacific during the LGM, which weakens trade wind stress and reduces the pressure gradient driving the throughflow (Ding et al., 2013; Fan et al., 2018; Rachmayani et al., 2025).

While the lgmDA v2.1 product provides a powerful, dynamically consistent framework for paleoclimate reconstruction, several inherent limitations must be considered when interpreting our results. First, the spatial reconstruction is inherently constrained by the heterogeneous distribution of the underlying proxy network (Tierney et al.) [2020]. Although the assimilation mitigates spatial sampling biases, the IMC's complex topography and oceanography may be under-resolved, particularly for the LGM when terrestrial proxy records are more abundant than marine ones. Our finding of reduced spatial variability during the LGM is a robust large-scale signal, but the product may struggle to fully capture the fine-scale heterogeneity that characterizes the modern IMC. Second, the reconstruction's fidelity is contingent on the accuracy of the prior model (iCESM1.2) and the proxy system models that translate geochemical measurements into climate variables. Biases in the model's representation of key regional processes, such as the ITF, monsoonal rainfall, or diurnal cycles, would propagate into the posterior estimates (Brady et al.) [2019; Tierney et al.] [2020]. Finally, while the offline ensemble Kalman filter approach is computationally efficient, it may not fully capture non-Gaussian uncertainties or non-linear error growth, potentially leading to an over-confident or overly smoothed reconstruction in a region known for its strong non-linear feedbacks.

Our information-theoretic analysis provides a quantitative measure of this regime shift. The higher Shannon entropy for LH SST indicates a more complex and heterogeneous spatial distribution, consistent with the modern, dynamic state of the IMC. In contrast, the lower ApEn (greater regularity) of LGM SST reflects a more uniform and predictable spatial pattern, reinforcing the interpretation of a climatically "locked" or less dynamic glacial state with a weakened and reconfigured ITF.

In summary, the stark statistical differences between the LGM and LH oceanographic distributions are signatures of a different climate mode. The glacial IMC was dominated by global ice age conditions that led to a cooler, saltier, and more homogenous ocean, driven by a weakened ITF, lower sea levels that disrupted freshwater pathways, a drier regional climate, and a more stratified water column. The transition to the LH saw the establishment of the modern, highly dynamic regime characterized by strong ITF influence, complex hydrology, and greater spatial heterogeneity.

5 CONCLUSION

Our statistical analysis suggests a fundamental reorganization of IMC oceanography between the LGN 636 and LH, characterized by distributional shifts that may extend beyond simple mean-state changes. The 637 LGM ocean appears to have been substantially cooler, saltier, and isotopically enriched relative to the LH, 638 with markedly reduced spatial heterogeneity across all three oceanographic variables. Nonparametric 639 hypothesis testing confirmed highly significant differences across multiple independent tests, with large effect sizes indicating that these likely represent profound changes in underlying distributional properties 641 rather than mere shifts in central tendency. These patterns possibly reflect the integrated effects of a weak-642 ened Indonesian Throughflow, lower sea level that exposed continental shelves and disrupted freshwater 643 pathways, enhanced vertical stratification, and a drier regional climate regime potentially associated with weakened monsoon circulation and southward displacement of the ITCZ. Information-theoretic complex-645 ity measures suggest that the LGM may have represented a more uniform, climatically "locked" state with reduced spatial variability, whereas the LH exhibits the dynamic, spatially heterogeneous oceanography 647 that characterizes the modern system. This statistical framework could provide useful constraints for validating paleoclimate model simulations and may help improve understanding of the sensitivity of 649 tropical Indo-Pacific circulation to glacial-interglacial boundary conditions, with potential implications for projecting future responses of this critical oceanic gateway to altered throughflow dynamics under 651 anthropogenic climate change. 652

653 ACKNOWLEDGEMENTS

This study was supported by the Dean's Distinguished Fellowship from the College of Natural and Agricultural Sciences, University of California, Riverside (2023) awarded to S.H.S.H., and by the Bandung Institute of Technology Research, Community Service and Innovation Program (PPMI-ITB 2025) awarded to F.K. and I.P.A.

AUTHOR CONTRIBUTIONS

D.Z.M.: Software, Formal Analysis, Data Curation, Visualization, Writing – Original Draft. S.H.S.H.:
 Conceptualization, Methodology, Software, Visualization, Formal Analysis, Supervision, Writing –
 Original Draft. I.P.A.: Conceptualization, Funding Acquisition, Supervision, Writing – Review & Editing.
 M. H.: Conceptualization, Supervision, Writing – Review & Editing. S. N. K.: Software, Writing –
 Original Draft. F.K.: Conceptualization, Funding Acquisition, Supervision, Writing – Review & Editing.
 R.R.: Supervision, Writing – Review & Editing.

OPEN RESEARCH

The Last Glacial Maximum Data Assimilation product (lgmDA v2.1) used in this study is publicly available through Zenodo at https://doi.org/10.5281/zenodo.5171432 and distributed under the GNU General Public License. All Python code used for statistical analysis, along with processed data and results, is available in the GitHub repository at https://github.com/sandyherho/stats_compare_imc_ocean_lgm_lh and released under the WTFPL license.

REFERENCES

671

Anderson, T. W. and Darling, D. A. (1952). Asymptotic Theory of Certain "Goodness of Fit" Criteria
Based on Stochastic Processes. *The Annals of Mathematical Statistics*, 23(2):193–212. https://doi.org/10.1214/aoms/1177729437.

Brady, E., Stevenson, S., Bailey, D., Liu, Z., Noone, D., Nusbaumer, J., Otto-Bliesner, B. L., Tabor, C., Tomas, R., Wong, T., Zhang, J., and Zhu, J. (2019). The Connected Isotopic Water Cycle in the Community Earth System Model Version 1. *Journal of Advances in Modeling Earth Systems*, 11:2547–2566. https://doi.org/10.1029/2019MS001663.

Clark, P. U., Dyke, A. S., Shakun, J. D., Carlson, A. E., Clark, J., Wohlfarth, B., Mitrovica, J. X.,
Hostetler, S. W., and McCabe, A. M. (2009). The Last Glacial Maximum. *Science*, 325:710–714.

https://doi.org/10.1126/science.1172873.

Cliff, N. (1993). Dominance Statistics: Ordinal Analyses to Answer Ordinal Questions. *Psychological Bulletin*, 114(3):494–509. https://doi.org/10.1037/0033-2909.114.3.494.

- Cover, T. M. and Thomas, J. A. (2006). *Elements of Information Theory*. Wiley-Interscience, Hoboken, NJ, 2nd edition. https://doi.org/10.1002/047174882X.
- D'Agostino, R. B. (1971). An omnibus test of normality for moderate and large size samples. *Biometrika*, 58(2):341–348. https://doi.org/10.1093/biomet/58.2.341.
- D'Agostino, R. B. and Pearson, E. S. (1973). Tests for departure from normality. Empirical results for the distributions of b_2 and $\sqrt{b_1}$. Biometrika, 60(3):613–622. https://doi.org/10.1093/biomet/60.3.613.
- DiNezio, P. N., Tierney, J. E., Otto-Bliesner, B. L., Timmermann, A., Bhattacharya, T., Rosenbloom, N., and Brady, E. (2018). Glacial changes in tropical climate amplified by the Indian Ocean. *Science Advances*, 4(12):eaat9658. https://doi.org/10.1126/sciadv.aat9658.
- Ding, X., Bassinot, F., Guichard, F., Fang, N. Q., Labeyrie, L., and Jian, Z. (2013). Indonesian Throughflow
 and monsoon activity records in the Timor Sea since the last glacial maximum. *Marine Micropaleon-tology*, 101:115–126. https://doi.org/10.1016/j.marmicro.2013.02.003.
- Epps, T. W. and Singleton, K. J. (1986). An omnibus test for the two-sample problem using the empirical characteristic function. *Journal of Statistical Computation and Simulation*, 26(3-4):177–203. https://doi.org/10.1080/00949658608810963.
- Fan, W., Jian, Z., Chu, Z., Dang, H., Wang, Y., Bassinot, F., Han, X., and Bian, Y. (2018). Variability of the Indonesian Throughflow in the Makassar Strait over the Last 30 ka. *Scientific Reports*, 8:5678. https://doi.org/10.1038/s41598-018-24055-1.
- Gaspari, G. and Cohn, S. E. (1999). Construction of correlation functions in two and three dimensions.

 Quarterly Journal of the Royal Meteorological Society, 125:723–757. https://doi.org/10.1002/qj.49712555417.
 - Gordon, A. L. (2005). Oceanography of the Indonesian Seas and Their Throughflow. *Oceanography*, 18(4):14–27. https://doi.org/10.5670/oceanog.2005.01.

707

717

718

- Gordon, A. L., Huber, B. A., Metzger, E. J., Susanto, R. D., Hurlburt, H. E., and Adi, T. R. (2012).

 South China Sea throughflow impact on the Indonesian throughflow. *Geophysical Research Letters*,
 39(11):L11602. https://doi.org/10.1029/2012GL052021.
- Hakim, G. J., Emile-Geay, J., Steig, E. J., Noone, D., Anderson, D. M., Tardif, R., Steiger, N., and Perkins, W. A. (2016). The last millennium climate reanalysis project: Framework and first results.

 Journal of Geophysical Research: Atmospheres, 121:6745–6764. https://doi.org/10.1002/2016JD024751.
- Hall, R. (2009). *Indonesia, Geology*, pages 454–460. University of California Press, Berkeley. https://doi.org/10.1525/9780520943728-104.
 - Hanebuth, T., Stattegger, K., and Grootes, P. M. (2000). Rapid Flooding of the Sunda Shelf: A Late-Glacial Sea-Level Record. *Science*, 288(5468):1033–1035. https://doi.org/10.1126/science [288.5468.1033].
- Hanebuth, T. J., Stattegger, K., and Bojanowski, A. (2009). Termination of the Last Glacial Maximum sea-level lowstand: The Sunda-Shelf data revisited. *Global and Planetary Change*, 66:76–84. https://doi.org/10.1016/j.gloplacha.2008.03.011.
- Harris, C. R., Millman, K. J., van der Walt, S. J., Gommers, R., Virtanen, P., Cournapeau, D., Wieser,
 E., Taylor, J., Berg, S., Smith, N. J., Kern, R., Picus, M., Hoyer, S., van Kerkwijk, M. H., Brett, M.,
 Haldane, A., del Río, J. F., Wiebe, M., Peterson, P., Gérard-Marchant, P., Sheppard, K., Reddy, T.,
 Weckesser, W., Abbasi, H., Gohlke, C., and Oliphant, T. E. (2020). Array Programming with NumPy.

 Nature, 585:357–362. https://doi.org/10.1038/s41586-020-2649-2.
- Hendrizan, M., Cahyarini, S. Y., Ningsih, N. S., and Rachmayani, R. (2021). Indonesian Throughflow Intensity and Sea Surface Temperature Anomaly since the Last Deglaciation: An Overview. *IOP Conference Series: Earth and Environmental Science*, 789:012053. https://doi.org/10.1088/1755-1315/789/1/012053.
 - 1755–1315/789/1/012053.
 Hoyer, S. and Hamman, J. (2017). xarray: N-D Labeled Arrays and Datasets in Python. *Journal of Open*
- Hoyer, S. and Hamman, J. (2017). xarray: N-D Labeled Arrays and Datasets in Python. *Journal of Open Research Software*, 5(1):10. https://doi.org/10.5334/jors.148.

 Jarque, C. M. and Bera, A. K. (1980). Efficient tests for normality, homoscedasticity and serial indepen-
- dence of regression residuals. *Economics Letters*, 6(3):255–259. https://doi.org/10.1016/ 0165-1765 (80) 90024-5.
- Jarque, C. M. and Bera, A. K. (1987). A Test for Normality of Observations and Regression Residuals. *International Statistical Review*, 55(2):163–172. https://doi.org/10.2307/1403192.

- Kageyama, M., Albani, S., Braconnot, P., Harrison, S. P., Hopcroft, P. O., Ivanovic, R. F., Lambert, 739 F., Marti, O., Peltier, W. R., Peterschmitt, J.-Y., Roche, D. M., Tarasov, L., Zhang, X., Brady, E. C., 740 Haywood, A. M., LeGrande, A. N., Lunt, D. J., Mahowald, N. M., Mikolajewicz, U., Nisancioglu, 741 K. H., Otto-Bliesner, B. L., Renssen, H., Tomas, R. A., Zhang, Q., Abe-Ouchi, A., Bartlein, P. J., Cao, 742 J., Li, Q., Lohmann, G., Ohgaito, R., Shi, X., Volodin, E., Yoshida, K., Zhang, X., and Zheng, W. 743 (2017). The PMIP4 contribution to CMIP6 - Part 4: Scientific objectives and experimental design of the PMIP4-CMIP6 Last Glacial Maximum experiments and PMIP4 sensitivity experiments. Geoscientific 745 Model Development, 10(11):4035-4055. https://doi.org/10.5194/gmd-10-4035-2017. Kolmogorov, A. (1933). Sulla determinazione empirica di una legge di distribuzione. Giornale dell'Istituto 747 Italiano degli Attuari, 4:83–91.
- Konecky, B. L., Russell, J. M., and Bijaksana, S. (2016). Glacial aridity in central Indonesia coeval 749 with intensified monsoon circulation. Earth and Planetary Science Letters, 437:15–24. https:// 750 //doi.org/10.1016/j.epsl.2015.12.037. 751
 - Kruskal, W. H. and Wallis, W. A. (1952). Use of Ranks in One-Criterion Variance Analysis. Journal of the American Statistical Association, 47(260):583-621. https://doi.org/10.1080/01621459. 1952.10483441.

753

754

761

768

769

774

775

- Lambeck, K., Yokoyama, Y., and Purcell, T. (2002). Into and out of the Last Glacial Maximum: sea-755 level change during Oxygen Isotope Stages 3 and 2. Quaternary Science Reviews, 21(1-3):343–360. 756 https://doi.org/10.1016/S0277-3791(01)00071-3. 757
- Larasati, O. D. D., Hendrizan, M., Rachmayani, R., and Napitupulu, G. (2024). Variability of Sea Surface 758 Temperature and Salinity in Makassar Strait During the Last Glacial Maximum. Bulletin of the Marine Geology, 39(2):111-121. http://dx.doi.org/10.32693/bomg.39.2.2024.882 760
- Lilliefors, H. W. (1967). On the Kolmogorov-Smirnov Test for Normality with Mean and Variance Unknown. Journal of the American Statistical Association, 62(318):399-402. https://doi.org/ 762 10.1080/01621459.1967.10482916.
- Malevich, S. B., Vetter, L., and Tierney, J. E. (2019). Global core top calibration of δ^{18} O in planktic 764 foraminifera to sea surface temperature. Paleoceanography and Paleoclimatology, 34(8):1292–1315. 765 https://doi.org/10.1029/2019PA003576. 766
 - Mann, H. B. and Whitney, D. R. (1947). On a Test of Whether One of Two Random Variables is Stochastically Larger than the Other. The Annals of Mathematical Statistics, 18(1):50-60. https: //doi.org/10.1214/aoms/1177730491.
- McKinney, W. (2010). Data Structures for Statistical Computing in Python. In *Proceedings of the* 770 9th Python in Science Conference, volume 445, pages 51-56. https://doi.org/10.25080/ 771 Majora-92bf1922-00a. 772
- Mood, A. M. (1954). Introduction to the Theory of Statistics. McGraw-Hill, New York. 773
 - Pincus, S. M. (1991). Approximate entropy as a measure of system complexity. Proceedings of the National Academy of Sciences, 88(6):2297–2301. https://doi.org/10.1073/pnas.88.6 2297.
- Rachmayani, R., Larasati, O. D. D., and Hendrizan, M. (2025). Thermocline Water Temperature Gradient 777 at the Indonesian Throughflow Pathways During Last Glacial Maximum (LGM). Bulletin of the Marine Geology, 40(1):13-27. http://dx.doi.org/10.32693/bomg.40.1.2025.937 779
- Romano, J., Kromrey, J., Coraggio, J., Skowronek, J., and Devine, L. (2006). Exploring Methods for 780 Evaluating Group Differences on the NSSE and Other Surveys: Are the t-test and Cohen's d Indices the 781 Most Appropriate Choices? In Annual Meeting of the Southern Association for Institutional Research, Arlington, VA. 783
- Schröder, J. F., Kuhnt, W., Holbourn, A., Beil, S., Zhang, P., Hendrizan, M., and Xu, J. (2018). Deglacial 784 Warming and Hydroclimate Variability in the Central Indonesian Archipelago. Paleoceanography and Paleoclimatology, 33(9):974-993. https://doi.org/10.1029/2018PA003323
- Scott, D. W. (2015). Multivariate Density Estimation: Theory, Practice, and Visualization. Wiley, New 787 York, 2nd edition. https://doi.org/10.1002/9781118575574. 788
- Shannon, C. E. (1948). A Mathematical Theory of Communication. Bell System Technical Journal, 27(3):379-423. https://doi.org/10.1002/j.1538-7305.1948.tb01338.xl 790
- Shapiro, S. S. and Wilk, M. B. (1965). An Analysis of Variance Test for Normality (Complete Samples). 791 Biometrika, 52(3/4):591-611. https://doi.org/10.2307/2333709 792
 - Silverman, B. W. (1998). Density Estimation for Statistics and Data Analysis. Routledge, New York.

```
https://doi.org/10.1007/978-1-4899-3324-9
```

796

- Smirnov, N. (1948). Table for Estimating the Goodness of Fit of Empirical Distributions. *Annals of Mathematical Statistics*, 19(2):279–281. https://doi.org/10.1214/aoms/1177730256.
- Solihuddin, T. (2014). A Drowning Sunda Shelf Model during Last Glacial Maximum (LGM) and
- Holocene: A Review. *Indonesian Journal on Geoscience*, 1(2):99–107. https://doi.org/10.799 17014/ijog.1.2.99-107.
- Stephens, M. A. (1974). EDF Statistics for Goodness of Fit and Some Comparisons. *Journal of the American Statistical Association*, 69(347):730–737. https://doi.org/10.1080/01621459.802 1974.10480196.
- Tardif, R., Hakim, G. J., Perkins, W. A., Horlick, K. A., Erb, M. P., Emile-Geay, J., Anderson, D. M., Steig, E. J., and Noone, D. (2019). Last Millennium Reanalysis with an expanded proxy database and seasonal proxy modeling. *Climate of the Past*, 15(4):1251–1273. https://doi.org/10.5194/
- Tierney, J. E., Malevich, S. B., Gray, W., Vetter, L., and Thirumalai, K. (2019). Bayesian Calibration of the Mg/Ca Paleothermometer in Planktic Foraminifera. *Paleoceanography and Paleoclimatology*, 34:2005–2030. https://doi.org/10.1029/2019PA003744.
- Tierney, J. E. and Osman, M. (2022). Last Glacial Maximum Data Assimilation (lgmDA) version 2.1.

 Documentation. https://doi.org/10.5281/zenodo.5171432.
- Tierney, J. E. and Tingley, M. P. (2014). A Bayesian, spatially-varying calibration model for the TEX₈₆ proxy. *Geochimica et Cosmochimica Acta*, 127:83–106. https://doi.org/10.1016/j.gca.814
- Tierney, J. E. and Tingley, M. P. (2018). BAYSPLINE: A new calibration for the alkenone paleother-mometer. *Paleoceanography and Paleoclimatology*, 33:281–301. https://doi.org/10.1002/ 2017PA003201.
- Tierney, J. E., Zhu, J., King, J., Malevich, S. B., Hakim, G. J., and Poulsen, C. J. (2020). Glacial cooling and climate sensitivity revisited. *Nature*, 584(7822):569–573. https://doi.org/10.1038/s41586-020-2617-x.
- Tjia, H. D. and Liew, K. K. (1996). Changes in tectonic stress field in northern Sunda Shelf basins. *Geological Society, London, Special Publications*. https://doi.org/10.1144/GSL.SP.1996. 106.01.19.
- Virtanen, P., Gommers, R., Oliphant, T. E., Haberland, M., Reddy, T., Cournapeau, D., Burovski, E.,
 Peterson, P., Weckesser, W., Bright, J., van der Walt, S. J., Brett, M., Wilson, J., Millman, K. J.,
 Mayorov, N., Nelson, A. R. J., Jones, E., Kern, R., Larson, E., Carey, C. J., Polat, İ., Feng, Y., Moore,
 E. W., VanderPlas, J., Laxalde, D., Perktold, J., Cimrman, R., Henriksen, I., Quintero, E. A., Harris,
 C. R., Archibald, A. M., Ribeiro, A. H., Pedregosa, F., van Mulbregt, P., and SciPy 1.0 Contributors
 (2020). SciPy 1.0: Fundamental Algorithms for Scientific Computing in Python. *Nature Methods*,
 17(3):261–272. https://doi.org/10.1038/s41592-019-0686-2.
- Voris, H. K. (2000). Maps of Pleistocene sea levels in Southeast Asia: shorelines, river systems and time durations. *Journal of Biogeography*, 27:1153–1167. https://doi.org/10.1046/j. 1365-2699.2000.00489.x.
- Whitaker, J. S. and Hamill, T. M. (2002). Ensemble data assimilation without perturbed observations.

 **Monthly Weather Review, 130:1913–1924. https://doi.org/10.1175/1520-0493 (2002)

 130<1913:EDAWPO>2.0.CO; 2.
- Wicaksono, S. A., Russell, J. M., Holbourn, A., and Kuhnt, W. (2017). Hydrological and vegetation shifts in the Wallacean region of central Indonesia since the Last Glacial Maximum. *Quaternary Science Reviews*, 157:152–163. https://doi.org/10.1016/j.quascirev.2016.12.006.
- Wilcoxon, F. (1945). Individual Comparisons by Ranking Methods. *Biometrics Bulletin*, 1(6):80–83. https://doi.org/10.2307/3001968.
- Xu, J., Holbourn, A., Kuhnt, W., Jian, Z., and Kawamura, H. (2008). Changes in the thermocline structure of the Indonesian outflow during Terminations I and II. *Earth and Planetary Science Letters*, 273(1–2):152–162. https://doi.org/10.1016/j.epsl.2008.06.029.